AIAA JOURNAL
Vol. 33, No. 12, December 1995

Structure of a Turbulent Double-Fin Interaction at Mach 4

Datta Gaitonde* and J. S. Shang†
U.S. Air Force Wright Laboratory, Wright–Patterson Air Force Base, Ohio 45433-7913

This paper examines the three-dimensional shock-wave/turbulent boundary-layer interaction in an inletlike geometry consisting of symmetrically placed 15-deg fins on a plate in an oncoming Mach 4 flow. Two different implicit numerical methods are employed to solve the full three-dimensional mean compressible Navier–Stokes equations: 1) a high resolution upwind scheme with the Baldwin–Lomax algebraic turbulence model and 2) the traditional Beam–Warming approach with a k–ϵ model. The comparison with experiment is very good for surface pressures, pitot pressure surveys, and surface shear patterns, although discrepancies with skin friction data are evident in the trailing portion of the interaction. Both computational schemes, despite major differences in modeling, predict similar flow structures in agreement with previous results at Mach 8. The flow is described in terms of a separated, nonreattaching boundary layer, a vortex interaction, longitudinal centerline vortices, and entrainment. The computed and experimental shock patterns are related to the streamline structure to provide a unified understanding of the flowfield.

I. Introduction

THE three-dimensional interaction of a shock wave with a turbulent boundary layer results in complex flow phenomena. Such interactions are ubiquitous in supersonic vehicle components, such as inlets and combustors. The features of the resulting flowfield are very interesting from a fundamental fluid dynamic standpoint. In addition, the practical consequences need to be accounted for in the design procedure because they are detrimental to the performance of aircraft at supersonic speeds.

An understanding of the dynamics of three-dimensional turbulent interactions is considerably facilitated through the use of simplified geometries that permit detailed examination of the mechanisms involved without prohibitive resource demands. Such configurations typically consist of a shock generator (e.g., a sharp or a blunt fin) mounted on a plate. The object of present interest is the double-fin configuration (Fig. 1), in which two opposed—in this instance symmetric—fins separated a finite distance are mounted on a flat plate. Each fin produces a shock whose strength depends on the fin angle, and this shock interacts with the boundary layer developing on the plate. The relevant flow parameters include the Mach and Reynolds numbers, the properties of the incoming boundary layer, the fin angles (or, alternatively, the shock strengths), the distance between the fins, and the wall thermal conditions.

The initial motivation to examine this inletlike geometry from a theoretical/computational standpoint stems from the observations of Mee and Stalker[1] who concluded based on experimental data that for a given oncoming boundary layer separation could be inhibited by achieving the desired pressure rise with a series of weaker intersecting shocks as opposed to a single stronger shock. Since boundary-layer separation is undesirable in many applications, a detailed study of this flow has potential design benefits.

The double-fin geometry represents a natural progression in physical complexity from the extensively examined single-fin configuration[2,3] that consists of a sharp wedge mounted on a flat plate. For strong single-fin interactions, such as those considered in Ref. 3, the principal mean flow feature is a vortical structure in agreement with the proposal of Kubota and Stollery.[4] Looking downstream, in the absence the right fin of Fig. 1, the dominant turning action of the vortical structure associated with the left fin is counterclockwise when viewed along the vortex axis from the intersection of the fin leading edge with the plate.

Received Jan. 30, 1995; revision received June 7, 1995; accepted for publication June 7, 1995. This paper is declared a work of the U.S. Government and is not subject to copyright protection in the United States.

*UES, Inc.; currently Visiting Scientist, Flight Dynamics Directorate, Computational Fluid Dynamics Research Branch, Aeromechanics Division. Senior Member AIAA.

†Senior Scientist, Flight Dynamics Directorate. Fellow AIAA.

Subsequent to the initial work of Mee and Stalker,[1] the double-fin flowfield has been examined numerically in several efforts (e.g., Refs. 5–7). In Ref. 6, the principal flow feature is described as "a low total pressure jet comprising two weakly counter-rotating vortices." An alternative approach employed in Ref. 7 describes the flowfield in terms of distinct flow regimes: a separated boundary layer, vortex interaction, a centerline vortex pair, and high-speed entrainment.

The numerical simulation of such complex fields has received much impetus from high-quality experiments.[8,9] In particular, Garrison and Settles[8,10] and Garrison et al.[11] have developed a sophisticated flowfield model based on a variety of experimental data over a range of interactions. The present work focuses on one of these configurations: a nominally Mach 4, 0.35-cm-thick boundary-layer interaction with shocks generated by 15-deg fins. The available experimental data for validation purposes include plate pressure and skin friction coefficients, pitot surveys, surface oil flow, and planar laser scattering images.

In addition to the flow control aspect of the problem, this geometry may be employed to examine fundamental phenomena in fluid dynamics, particularly, 1) the interaction of the two vortical structures induced by the two individual fins and 2) three-dimensional separation in the neighborhood of a symmetry plane. The fluid structures possible due to such events exhibit a high degree of complexity. The anticipated vortical structure induced by the right fin is clockwise when viewed along its axis from the intersection of this fin leading edge with the plate, i.e., the two vortical structures are mirror images of each other about the symmetry plane. Thus, the rotation implied by both structures in a plane normal to the spanwise direction is similar and is in the same sense as that of the vorticity in the upstream two-dimensional boundary layer. Although the present work describes the structure near the symmetry plane as an interaction of two distinct vortices, as will be discussed later, vortex lines in the

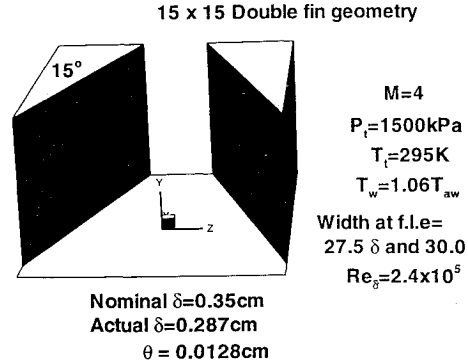

Fig. 1 Double-fin configuration, where f.l.e is fin leading edge.

flow are continuous and point in the general direction from the right fin to the left. Consequently, an alternative single vortical viewpoint is also feasible.

The objectives of this work are 1) to examine the structure of the interaction at Mach 4 and to compare with previous results at Mach 8, 2) to examine the sensitivity of this structure to turbulence modeling, 3) to describe the shock structure and to compare this with experimental observation, and 4) to relate the shock and streamline structures to provide a more complete understanding of the flow physics.

To achieve these objectives, two popular methods are utilized, one combining a high-resolution scheme with an algebraic turbulence model and the other a classical central difference scheme with a two-equation turbulence model modified to include a compressibility correction (Sec. II). Details of the calculations, including mesh resolution studies to estimate solution dependence on spatial resolution are presented in Sec. III. The results (Sec. IV) first validate the computations by comparison with experimental data. The streamline and shock structures of the flowfield are then discussed. The paper concludes after describing the interrelationship between the streamline and shock patterns.

II. Theoretical Model

The full three-dimensional compressible Navier–Stokes equations in strong conservation form and mass-averaged variables are solved on a curvilinear coordinate system. The viscous fluxes are discretized with a central difference stencil. The molecular viscosity is derived from Sutherland's law, whereas the eddy viscosity is obtained from each of two turbulence models as described next.

In the Roe/Baldwin–Lomax (RBL) method, the inviscid fluxes are discretized with Roe's flux-difference split scheme implemented in a cell-centered finite volume approach. Higher order accuracy is obtained in smooth regions using the monotonic upwind-centered scheme for conservation laws (MUSCL) formulation in conjunction with van Leer's limiter to preserve monotonicity. Both second- and third-order accurate approaches are examined. A mesh- and flow-based eigenvalue cutoff is employed to enforce the entropy condition.[7] The implementation of the Baldwin–Lomax model requires specification of appropriate length scales that are ambiguous in the vicinity of a corner such as at the fin–plate juncture. In the present work, the inverse blending (IB) procedure is implemented to address this issue. Time integration is achieved with an implicit residual driven line Gauss–Seidel relaxation scheme. Numerical details of this method may be found in Ref. 7.

In the Beam–Warming/k–ϵ (BKE) approach, a first-order time-accurate approximate factorization procedure is utilized with a central difference plus dissipation algorithm. Details of the implementation, including the k–ϵ equations and the compressibility correction of Sarkar et al. may be found in Ref. 12.

III. Description of Computations

The flow parameters are chosen to duplicate experimental data.[10,13] The freestream conditions are flow at Mach 4, Reynolds number of 80×10^6/m, stagnation pressure of 1500 kPa, and stagnation temperature of 295 K. The properties of the boundary layer entering the interaction are specified as $\delta = 0.287$ cm, $\delta^* = 0.0950$ cm, and $\theta^* = 0.0128$ cm. Quantitative experimental data consists of surface pressure and skin friction coefficient measurements on the plate as well as pitot pressures on a crossflow plane, whereas qualitative results are available in the form of surface oil flow and planar laser scattering images. The width of the channel at the fin leading edges is 9.63 cm except for C_f measurements for which it is 10.5 cm. Since quantitative validation is an important part of this effort, calculations are performed at both widths as specified subsequently. Also, in keeping with the practice of Ref. 13, the nominal boundary-layer thickness ($\delta_{\text{nom}} = 0.35$ cm) is employed for normalization purposes.

The coordinate system is aligned so that x points in the downstream direction, y is plate normal, and z is spanwise. The origin is on the symmetry plane at the streamwise location corresponding to the fin leading edge. The condition of symmetry is invoked on the central plane and, thus, only the right-half of the domain (looking downstream) is calculated. In the configuration examined by Garrison et al.,[11] the fins end abruptly. To simulate any effects of the trailing-edge expansion in the computed solution, in some of the calculations to be presented, a duct is appended to the end of the domain. The effect on the solution in the region of interest is insignificant, substantiating the conclusions of negligible upstream influence of the fin trailing edges made in Ref. 10.

The boundary conditions may be summarized as follows. On both solid surfaces (fin and plate), the no-slip condition is enforced, the wall temperature is specified based on experimental data ($T_{\text{wall}} = 1.06T_{\text{adiabatic,wall}}$), and the normal pressure gradient is assumed zero in accordance with boundary-layer theory. At the upstream end of the domain, the momentum thickness of the incoming boundary-layer profile is matched with the experimental value. This profile is generated independently with two-dimensional codes based on the Baldwin–Lomax model[14] for the RBL method and on the k–ϵ model[15] for the BKE method. The downstream and top boundaries are assumed to be far enough away for the application of simple zero-gradient extrapolation. Symmetry conditions are applied on two planes, one upstream of the fin leading edge and the other equidistant between the two fins. In the absence of any qualification, the term symmetry plane refers to the latter. The flow in the neighborhood of this symmetry plane is one of primary interest. Special care is taken to prevent contamination of the solution in this region due to the larger stencil of the fourth-order dissipation operator in the BKE method. Five points are appended to the domain on the left side of the plane of symmetry. The flow conditions at these points are derived from their mirror points inside the domain with the spanwise velocity appropriately reversed.

The grids are generated as a sequence of nonuniform Cartesian planes normal to the direction of the upstream flow. In each plane, the grid is clustered in the vicinity of the solid boundaries to provide adequate resolution of the boundary layer. The mesh density is also increased near the symmetry plane. A total of five calculations are described on three meshes, whose dimensions are indicated in Table 1. Mesh A spans the narrower channel width of 9.63 cm and is designed to be adequate for the RBL method based on a mesh resolution study presented in an earlier work.[7] Three calculations are described on this mesh: 1) second-order RBL (RBL-SO), 2) third-order RBL (RBL-TO), and 3) BKE. Mesh B is similar to A but spans the wider channel width (10.5 cm). The body normal and streamwise spacing are the same, but some reduction in mesh density is obtained in the spanwise direction. Only the BKE method is computed on mesh B. For the BKE method, grid resolution criteria are unavailable for the present type of flow. For this reason, the BKE method is also computed on a finer grid (mesh C). Although the additional number of points in mesh C is only 35% greater, the

Table 1 Grid size and mean spatial resolution

Mesh	$IL \times JL \times KL$	w^a/δ	$\Delta x/\delta$	$\Delta y/\delta$	$\Delta z/\delta$	MD[b] ($/\delta^3$)	Calculations (y^+)[c] RBL-SO	RBL-TO	BKE
A	$99 \times 88 \times 99$	27	0.47	0.15	0.14	134	√[d](1.08)	√(1.08)	√(1.05)
B	$99 \times 88 \times 99$	30	0.47	0.15	0.17	131	NC[e]	NC	√(1.05)
C	$115 \times 89 \times 115$	30	0.35	0.12	0.13	200	NC	NC	√(0.8)

[a]The symbol w = channel width at the fin leading edge.
[b]MD is mesh density (points per volume).
[c]The symbol y^+ = height of first point on plate in wall units.
[d]√ indicates computed.
[e]NC indicates not computed.

mesh density is disproportionately increased (50%) because the domain size is reduced both in the streamwise (the region downstream of the fin trailing edge is not computed) and in the plate-normal directions. In addition, most of the extra points are focused in the region of interest near the symmetry plane. Mean values of y^+ are presented in Table 1 and satisfy guidelines generally recommended for each turbulence model ($y^+ < 3$ for BL, $y^+ \leq 1$ for k–ϵ).

Convergence is determined for all computations by monitoring several quantities including the residual of the flow vector, surface pressure, and heat transfer rates, as well as integrated root mean square measures of several quantities on the plate.

IV. Results

The computations are first validated by comparison with experimental data. The discussion of flow physics is accomplished by describing the streamline and shock structures. These are then correlated with several salient aspects of the flowfield.

A. Validation of Computed Results

The computed results are validated by comparison with the experimental data of Garrison and Settles as presented in Ref. 13. The pressure distribution on the plate centerline is plotted in Fig. 2a. The abscissa is the streamwise distance normalized by the nominal boundary-layer thickness ($X = x/\delta_{\text{nom}}$, $\delta_{\text{nom}} = 0.35$ cm), whereas the pressure is normalized by its freestream value ($P = p/p_\infty$). Three calculations are plotted, all on mesh A since for static pressure measurements, the width of the experimental configuration was 9.63 cm. The first two curves are results with the second- and third-order RBL formulations, whereas the third curve is with the BKE method. All computations show the experimental trend of monotonically increasing pressure until the rear of the domain where the expansions from the trailing edges of the fins cause a drop in surface pressure. The RBL method underpredicts the upstream influence by a significant amount, though little difference is evident between the second- and third-order formulations. The BKE method is highly accurate in predicting the upstream influence as well as the sharp initial pressure rise. The subsequent discussion will show that this flow is sufficiently resolved on this mesh. Along the entire centerline, there is only a modest overprediction in the surface pressure. The pressure

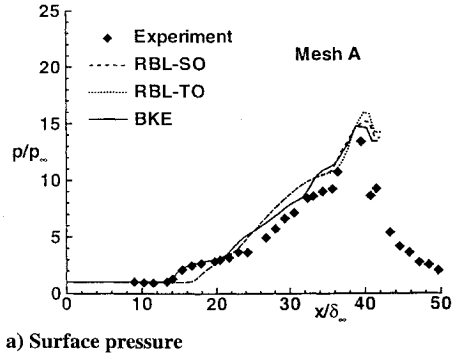

a) Surface pressure

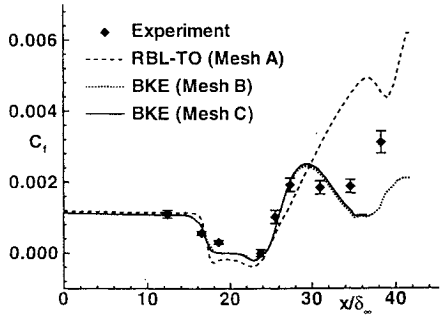

b) Skin friction coefficient

Fig. 2 Validation: surface pressure and skin friction coefficient on plate centerline, second order SO, third order TO, centerline CL, Roe/Baldwin–Lomax RBL, and Beam–Warming/k–ϵ BKE.

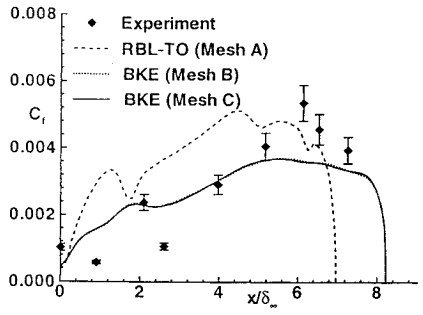

Fig. 3 Validation: skin friction coefficient on spanwise cut at $X = 25.3$, third order TO, Roe/Baldwin–Lomax RBL, Beam–Warming/k–ϵ BKE.

near the trailing end of the plate is strongly influenced by features associated with the viscous–inviscid interaction as discussed later.

The centerline skin friction coefficient is presented in Fig. 2b. The experimental data is plotted with error bounds as specified by the experimentalists. Three calculations are plotted, the third-order RBL method on mesh A and the BKE method on meshes B and C. The last two employ the correct experimental channel width, whereas the first is on the narrower geometry and is presented mainly to observe the trends with the RBL method. In the upstream undisturbed boundary layer, the computed skin friction coefficient is within the experimental error. All calculations show separation of the centerline boundary layer as indicated by the negative skin friction values. This is in agreement with the experimental data.[16] The calculated separation point and the size of the reversed flow region are also in good agreement. With the RBL method, however, this is fortuitous. In fact, since the RBL calculation employs a narrower channel, this agreement is actually indicative of the underprediction of the upstream influence, a trend observed earlier with the surface pressure as well. After attachment, however, the advantage clearly falls to the BKE method, which correctly predicts the rapid rise in skin friction in the developing boundary layer. The experimental data then reach a plateau that is not reproduced by any calculation. The BKE method does, however, show a peak followed by a lowering of C_f below experimental values before recovery. In contrast, the RBL method shows a generally monotonic increase in skin friction coefficients. There is no significant difference in the values obtained with BKE on the two meshes, implying that a reasonable level of mesh resolution has been achieved.

The prediction of skin friction coefficient along a spanwise cut is shown in Fig. 3. The abscissa in this figure is the spanwise coordinate ($Z = z/\delta_{\text{nom}}$) measured from the symmetry plane that corresponds to $Z = 0$. Note again that the fin/plate juncture occurs at $Z \sim 7$ with RBL because of the narrower channel width, whereas that with the BKE method occurs at $Z \sim 8.25$. All calculations show the rapid rise near the corner, though underpredicting the experimental values. In the region $3 < Z < 6$, the C_f values with the BKE method fall within the experimental range. The experimental data show interesting features near the symmetry plane ($0 < Z < 3$). An oscillatory trend is observed with local maxima at $Z \sim 0$ (symmetry plane) and $Z \sim 2.1$, whereas minima are observed at $Z \sim 0.9$ and $Z \sim 2.8$. At this streamwise location, this variation is not reproduced by any calculation. As discussed later, these local extrema are associated with coherent flow features that are reproduced in the computational results only at farther downstream locations. In the simulation, the maximum at the symmetry plane arises because of flow attachment, whereas, moving away from the symmetry plane, the two minima are associated with secondary flow separation and a shock-wave/boundary-layer interaction, respectively. In fact, since the RBL method employs a narrower channel width, the curve plotted is equivalently at a location farther downstream, and one minimum is observed at $Z \sim 2$ corresponding to the shock-wave/boundary-layer interaction.

Despite the poor prediction of C_f in some regions, the agreement with available measurements of the flow above the plate surface is very good. Figure 4 shows the computed (BKE, mesh C) and measured pitot pressures normalized by the freestream stagnation pressure in the $X = 32.33$ plane. Note that the experimental data do not extend to the surfaces. The classical numerical method smears

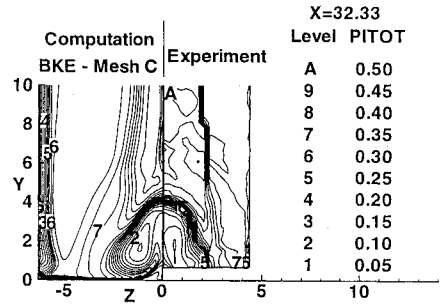

Fig. 4 Validation: pitot pressure normalized by freestream stagnation pressure on $X = 32.33$ plane, Beam–Warming/k–ϵ model.

the shock wave in the inviscid regions. Nevertheless, the features of the interaction are accurately reproduced. The dominant structure in both experiment and computation is the low pitot pressure region near the center of the channel. The physical details revealed in this figure and the relationship to the overall flow pattern are presented later.

In summary, with the exception of skin friction data in some regions, the BKE method shows very good agreement for surface pressure and flowfield surveys of pitot pressure. The RBL method, although slightly inferior to the BKE method in surface comparison, successfully reproduces most trends in experimental data. In addition, as will be demonstrated later, both methods reproduce the experimentally observed features in surface streamlines. The RBL method further shows very good agreement with the experimental shock structure. The discrepancies in skin friction data comparison are consistent with those of previous research efforts in similar shock-wave/boundary-layer interactions where derivative quantities linked to the viscous stresses (also including heat transfer rates) have shown poor agreement, whereas the overall structure of the flow itself has been correctly reproduced.[6,7,16] These findings reiterate that the effects of inadequacies in turbulence modeling for such flows are restricted mainly to regions very close to the walls. The dominant features of the flowfield are primarily inviscid rotational and are adequately represented by the simulation as presented subsequently. In this respect, the surface shear pattern discussed next is merely the footprint of the vortical structure of the field.

B. Streamline Structure

The experimental surface streamline schematic is reproduced with permission from Ref. 10 in Fig. 5a. The computations are plotted in Figs. 5b and 5c with RBL and BKE, respectively. Several special lines are readily evident in both calculations: primary line of separation/coalescence (PLS), primary line of attachment/divergence (PLA), secondary line of separation/coalescence (SLS), and centerline of attachment/divergence (CLA). There is reasonably good agreement between computation and experiment. The equivalence of PLS with primary separation (PS), PLA with primary attachment (PA), and CLA with centerline attachment (CA) is clear. The principal difference lies in the computed line marked SLS that in the experimental sketch is replaced by three different lines of coalescence—PS, secondary separation (SS), and centerline separation (CS)—that have merged together downstream. SLS (computed) may be identified with the experimental SS or CS in this region. However, the experimental CS "spans the interaction centerline,"[10] whereas in the computation, SLS originates downstream of the intersection of the two PLSs and is not directly connected to its counterpart on the other side of the plane of symmetry. Also, the experimental SS starts much farther upstream than observed in the calculation.

The observed differences between the two computations are mainly qualitative. The principal practical difference lies in the separation distance between CLA and SLS (Figs. 5b and 5c) that as will be evident later demarcates the size of a pair of centerline longitudinal vortical structures on either side of the symmetry plane. Although it is difficult to make quantitative estimates, for the same fin width (9.63 cm), both computations, but especially RBL,

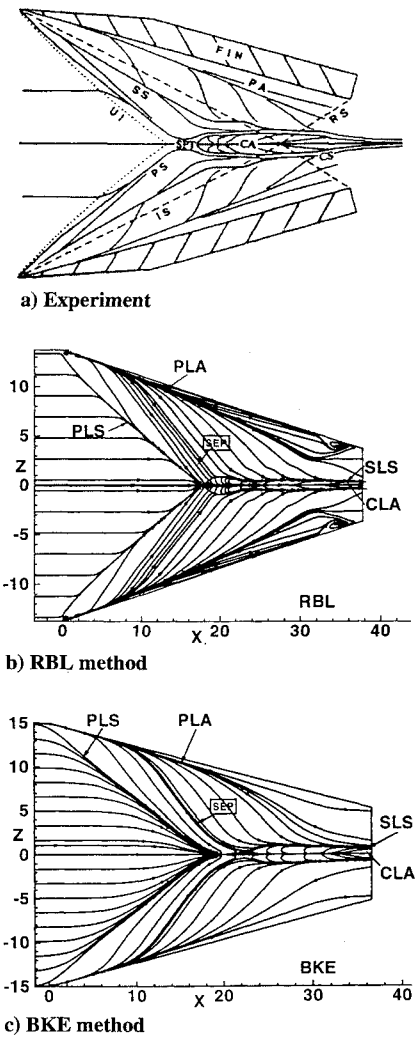

Fig. 5 Surface streamline patterns: experiment of Ref. 10 reproduced with permission; primary line of separation PLS, primary line of attachment PLA, secondary line of separation SLS, centerline of attachment CLA, and separatrix segment SEP.

underpredict the distance between SLS and CLA—a trend observed to a greater extent in a previous Mach 8 flow.[7]

The topological character of the manner in which fluid separates from the symmetry plane is described in Ref. 17 in terms of critical points on the plate and within the flow, i.e., points where the velocity is zero and has indeterminate direction. Those results are not reproduced here for brevity. It is noted here, however, that the detailed structure is similar to that obtained for the Mach 8 interaction of Ref. 7 and is closely related to a theoretically predicted bifurcation derived in Ref. 18.

The kinematic structure of the three-dimensional flowfield is now discussed with the help of particle paths. To derive a coherent structure, the release points of the particles are chosen in such a manner that they arrive close to each of the several lines of separation and attachment just examined. The different particle traces are then joined to form ribbons. With this approach, both theoretical methods show a similar structure, which resembles previous results with the RBL method at Mach 8.[7] For completeness, this description is reiterated, but for brevity the ribbon structure with only the BKE method is presented.

Figure 6a displays the four coherent features of the computed flowfield. Note that an artificial aspect ratio has been applied to highlight the various features.

First is separated boundary layer (BL). The entire upstream boundary layer separates (primary separation) from the plate and does not reattach. The sweep angle toward the centerline of particles separating near the fin leading edges is large, while it is zero on the symmetry plane. This surface of separation is thus broad upstream

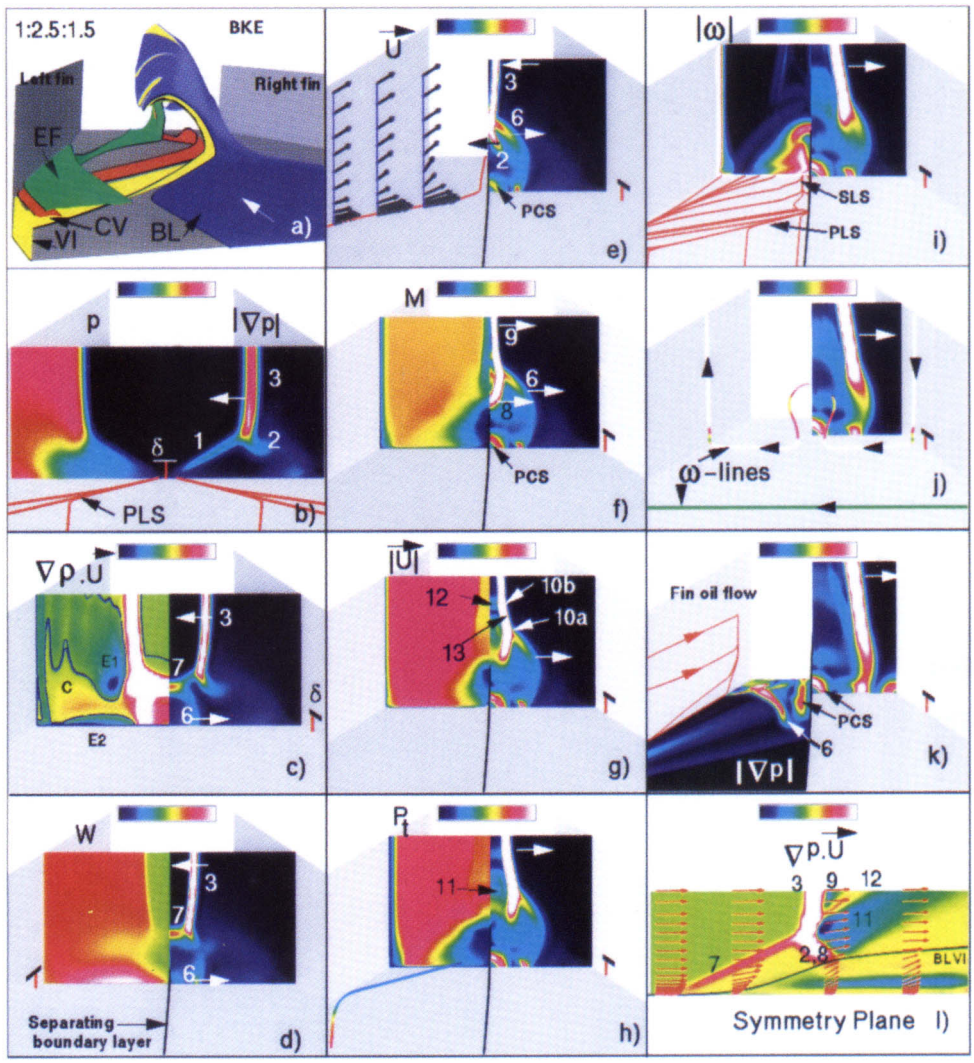

Fig. 6 Structure of flow: a) ribbon structure, b–k) shock structure with $|\nabla p|$ on right portion of each frame, and l) $\nabla p \cdot U$ on symmetry plane, select velocity vectors, and the BLVI shear layer. See Table 2 for variable and range of quantity plotted on left portion. See Table 3 for key to numerically identified features.

but becomes relatively narrow downstream. Also, the profile of the surface changes from flat upstream to curved downstream with significantly more curvature compared to the higher Mach, narrower channel case of Ref. 7. The region beneath the separated boundary layer is occupied by the following features.

Second is the vortex interaction flow (VI). Fluid attaching near the corner but just downstream of the fin leading edge sweeps spanwise and separates from the downstream side of the separated boundary layer. The shear layer formed by the separated boundary layer and the vortex interaction flow will be denoted BLVI. The vortex interaction regime results in one or more off-surface stagnation points on the symmetry plane as described in Ref. 17.

Third is the centerline vortex flow (CV). Some fluid, also originating near the fin leading edges, sweeps spanwise toward the symmetry plane and is turned streamwise by it to form two mirror counterparts of a centerline vortex.

The fourth is the entrainment flow (EF). High-energy fluid from the essentially inviscid regions near the fin leading edges attaches near each corner, sweeps across the channel and separates prior to reaching the centerline. The sense of rotation of this regime is counter to that of the centerline vortex on the same side of the symmetry plane.

The flow structures presented in Fig. 6a may be correlated with the plate pattern. The fluid adjacent to the plate in the oncoming boundary layer separates at the PLS. The region underneath is occupied by the spanwise movement of the flow attaching to the PLA. The portion of the flow whose footprint lies between the PLS and the separatrix (marked SEP in Fig. 5), after attaching to the PLA, separates from the downstream side of the PLS, and constitutes the vortex interaction regime. The entrainment flow attaches at PLA at larger distances downstream of the fin leading edge, traverses the spanwise length of the domain, and separates from the fin side of SLS. Fluid bounding the CV also originates near the fin leading edge, and after crossing the channel half-width is turned by the symmetry plane, attaches at CLA, and then separates from the symmetry plane side of SLS.

C. Shock Structure

Garrison and Settles[10] have developed a sophisticated model to describe the three-dimensional shock structure of crossing shock interactions based on extensive planar laser scattering data. The choice in the present work of a high-resolution discretization scheme, viz., the RBL method, provides a unique opportunity to examine the computed shock structure. The turbulence model is not expected to be a significant issue in this endeavor because the primary focus of this task is on regions relatively far away from the solid boundaries where, from the arguments of the Sec. IV (see also Refs. 6 and 7), the flow exhibits the characteristics of an inviscid, rotational field.

The shock pattern in crossing shock turbulent flowfields is highly three dimensional. An examination of this structure is facilitated by examining the trace of the shock intersection on a sequence of cutting planes aligned with the crossflow ($X = \text{const}$), such as shown in the right portion of Figs. 6b–6k. A number of variables are suitable to examine the trace of the shock, including static pressure, density or total pressure. Figure 6b shows the static pressure on the left side at a streamwise station $X = 16.59$ from the fin leading edge and the

Table 2 Color spectrum ranges of variables in Fig. 6

Frame	X	Quantity	
		Left	Right
a	——	Stream surface structure	
b	16.59	$1 < p < 4.5$	$0 < \|\nabla p\| < 4.54$
c	21.96	$-0.1 < \nabla\rho \cdot \boldsymbol{U} < 0.1$	$0 < \|\nabla p\| < 4.54$
d	23.36	$-0.53 < W < 0.53$	$0 < \|\nabla p\| < 4.54$
e	25.34	$\boldsymbol{U}$	$0 < \|\nabla p\| < 4.54$
f	27.06	$1 < M < 4$	$0 < \|\nabla p\| < 4.54$
g	28.06	$0.45 < \|U\| < 1$	$0 < \|\nabla p\| < 4.54$
h	28.87	$1 < P_t < 142$	$0 < \|\nabla p\| < 4.54$
i	30.34	$0 < \|\omega\| < 0.52$	$0 < \|\nabla p\| < 4.54$
j	31.47	ω lines	$0 < \|\nabla p\| < 4.54$
k	32.73	$0 < \|\nabla p\| < 4.54$	$0 < \|\nabla p\| < 4.54$
l	——	Symmetry plane: $\nabla p \cdot \boldsymbol{U}$, $\boldsymbol{U}$, BLVI	

Key: p = static pressure, ρ = density, U = Cartesian velocity vector, W = spanwise velocity, M = Mach number, P_t = stagnation pressure, ω = vorticity vector, BLVI = boundary layer, vortex interaction shear layer. Normalization: U_∞, p_∞, ρ_∞, δ_{nom}.

quantity $|\nabla p|$ i.e., the magnitude of the three-dimensional pressure gradient on the right. The primary line of separation is marked on the plate. The height of the nominal boundary layer is also shown in order to provide a length scale. It is evident that $|\nabla p|$ emphasizes the shock structure. This advantage of $|\nabla p|$ over p is crucial in examining the complex shock-crossing region downstream. The right portions of the frames of Figs. 6b–6k therefore display $|\nabla p|$. The complete shock structure in the spanwise channel may be obtained by mentally reflecting the $|\nabla p|$ pattern across the symmetry plane. The left portion of each frame shows various features to be discussed later. The ranges for the variables plotted in these frames are indicated in Table 2.

It is important to note that the arrows in Fig. 6 on the various shocks as well as terms denoting shock movement refer to the apparent motion of the shock trace as the cutting plane is moved infinitesimally downstream. Neither has temporal significance. Further, because of space constraints in Fig. 6, some features are not marked where they first appear.

Focusing on the right sides of each frame of Fig. 6, at $X = 16.59$ (frame Fig. 6b), the interaction is similar to that for a single fin and the dominant shock feature is the primary λ structure comprising the separation, and the rear and inviscid shocks.[19] These are marked 1, 2, and 3, respectively. The terms primary and reflected will be employed for shocks before and after reflection from the symmetry plane. The numerical notation closely follows that of Ref. 10 for ease of comparison with the experimental model. To retain notational consistency, some features of Ref. 10 are not shown but are mentioned. The numerical designators employed for each feature are summarized in Table 3. In the Fig. 6b frame, the region between 3 and the fin is the downstream side (i.e., the fluid here has already passed through the shock) whereas that between 3 and the symmetry plane is the upstream side. In this sense, shocks move into the locally upstream fluid. Further, relative to the upstream flow, shocks impart velocity on the downstream fluid in the same direction as their motion. Also observed in this crossflow plane but not shown are: 1) a slip line (feature 4) spanning the distance from the triplepoint to the fin/plate corner and 2) a separation vortex (5) beneath the λ structure.

Proceeding downstream, in the Fig. 6c frame ($X = 21.96$), 1 reflects off the symmetry plane. The process has been characterized as an irregular Mach reflection[10] forming a Mach stem (7) at the symmetry plane, and a curved reflected separation shock (6). In the Fig. 6d frame, 6 and 2 are coincident, the former moving away from the symmetry plane, the latter toward it. In the Fig. 6e frame, 6 and 2 cross each other and are visible as separate entities. Details of the shock structure in this region are difficult to discern since the action of the limiter lowers the local order of accuracy. In addition, the mesh is relatively coarse in comparison with that in the boundary layers, further complicating shock recognition. Based upon a close examination of the flow between the Fig. 6e and 6f frames, the sequence described in Fig. 7 appears to exist.

At the Fig. 6e frame, two distinct but very closely located triplepoints are shown in sequence II of Fig. 7, which exaggerates the actual computational situation where the four shocks (2, 7, 6, and 3) are compressed to only a few points in each direction. The triplepoint associated with 7, 2, and the distorted inviscid shock 3 then moves toward the symmetry plane, thus marking the end of 7 to obtain sequence III. It is postulated that the point of intersection of the shock system with the symmetry plane then moves upward rapidly while the triplepoint associated with 6 moves toward the symmetry plane to form a common intersection of the three shocks (3, 6, and 2) as shown in the sequence IV. This rearrangement ends the distorted portion of 3 that at this point curves slightly toward the symmetry plane—a characteristic observed to a lesser extent in earlier frames (e.g., Fig. 6c frame). After this, both 3 as well as 2 reflect off the symmetry plane, giving rise, considering both sides of the plane of symmetry, to a diamond-shaped high-pressure region with two points of intersection on the symmetry plane (sequence V). This brief dual intersection is also observed in the shock structure on the symmetry plane as discussed later. The pattern at the inviscid shock intersection point is sketched in sequence VI, whereas VII and VIII highlight the structure in the Fig. 6f and 6g frames.

The Fig. 6f frame shows the shock structure after 2 as well as 3 reflect to form the reflected rear shock (8) and the reflected inviscid shock (9), respectively. Downstream of the inviscid shock intersection, all shocks move away from the symmetry plane in the form of a distorted λ. Note, however, that in contrast to the Fig. 6b frame (for example), fluid between the inviscid shock and the symmetry plane in the Fig. 6f frame is downstream of the two inviscid shocks (3 and 9), whereas that between 9 and the fin has only been processed through 3. Reflected separation shock 6 is relatively strong in two locations, near the triplepoint of the reflected λ and also at its foot. Further, a new shock structure appears [plate centerline structure (PCS)], clearly unrelated to the λ and generates a tunnel of high static pressure in the center of the channel and near the plate.

In the Fig. 6g frame, several additional features are clearer. Between 9 and the symmetry plane, a centerline shock (12) is observed, as is a diffuse gradient identified in the Fig. 6h frame as an expansion (11). The Fig. 6g frame also shows two distinct triplepoints, the

Table 3 Numerical notation employed in description of shock structure

Description	Number designator
Primary separation shock	1
Primary rear shock	2
Primary inviscid shock	3
Slip line (not shown)	4
Separation vortex (not shown)	5
Reflected separation shock	6
Mach stem	7
Reflected rear shock	8
Reflected inviscid shock	9
Triplepoint	10(a, b)
Expansion	11
Centerline shock	12
Bridge shock	13
Rolled up slip lines (not shown)	14
Plate centerline structure	——

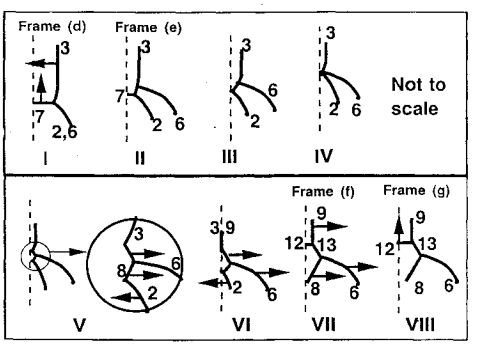

Fig. 7 Schematic sketch of reflection of incident triple point from symmetry plane.

lower one denoted 10a at the intersection of 6 and 8, and the other denoted 10b at the intersection of 12 and 9. The two triplepoints are connected by a bridge shock 13.

Proceeding further downstream, the Fig. 6h–6j frames display several trends. 1) The strength of 6 diminishes near the triplepoint, though it increases near the plate. 2) The trace of 8 moves much faster than 6, i.e., 8 forms a larger angle with the streamwise direction than 6, and the two merge between the Fig. 6i and 6j frames beyond which point the lower triplepoint 10a cannot be discerned. 3) The triplepoint 10b and 12 move upward, 12 weakening significantly in the process. 4) The high-pressure region over the PCS remains unaltered. In the final Fig. 6k frame, the combined reflected shocks (6, 9, and 8) join what is evident from earlier frames as the foot of 6. Additionally, near the corner, a new high-pressure-gradient region is observed. Beyond this spanwise section, the shock system interacts with the fin boundary layer and also the expansion from the fin trailing edges. These features are explained and correlated with the other aspects of the flow in later paragraphs.

The present results agree fairly well with the experimental model of Garrison and Settles. The principal differences occur after the reflection of the entire λ pattern from the symmetry plane (Fig. 6g frame). In the experiment, the distorted λ retains its structure at least until the reflected separation shock 6 impinges on the fin, whereas in the computation, the reflected system merges to form a single entity prior to impingement on the fin. Also, in the experiment, the high-pressure region near the corner (Fig. 6k frame) is not explicitly noted. The experimental flow visualization on the fin surface, however, indicates the intersection of 6 near the juncture at a location upstream of the impingement of the inviscid shock on the fin.[11] The relatively high strength of the foot of the reflected separation shock (6) is also not noted in the experimental description. Finally, an attempt was made to analyze the computed slip line structure with several variables. The calculated structure matches experiment until the location where the Mach stem (7) vanishes. Despite the use of a high-resolution scheme, no definitive conclusions can be drawn in the postinviscid shock reflection region because of the relatively coarse nature of the mesh in these essentially inviscid regions. A comparison with previous computations[11] with the present flow parameters reveals good agreement in the initial portion (until the Fig. 6d frame). However, the subsequent computed shock structure described in Ref. 11 does not contain the presence of 6 as a distinct feature. The high-pressure region near the PCS has been noted in previous computations[6,7] and experiment[11] and its genesis is presented next.

D. Discussion of Flow Physics

Figure 6 is now revisited to further examine the flowfield. In the initial region of the interaction, the flowfield structure resembles that of two single fins. The dynamics of the double-fin interaction is closely linked to the single-fin flowfield, which has been examined in great detail both from three-dimensional as well as quasiconical perspectives (for example, see Ref. 20 and references therein). The flow description of Ref. 20 includes a (primary) vortex, an expansion over and around the vortex, and jet impingement. Some of these features may be easily identified in terms of the flowfield model presented earlier. The primary vortex of Ref. 20 is constituted by a combination of what has been described in this work as the separated boundary layer, the vortex interaction, and the entrainment flows. Indeed, for the single fin, in the absence of secondary separation such as described in Ref. 19, there is no distinction between the vortex interaction and entrainment flow regimes. Both attach at the PLA and separate from the downstream side of the PLS, which for the single-fin, extends semi-infinitely away from the fin–plate apex.

The identification of expansions and compressions in a crossflow plane in the early portion of the interaction sheds much light on subsequent developments. Since the direction of fluid motion is not accounted for, neither $|\nabla p|$ nor static pressure shown in the Fig. 6b frame by themselves permit differentiation between smoother compressions and expansions, though sharp features can be identified as shocks. The local velocity may be incorporated in the analysis in a straightforward manner by examining the substantial derivative $(\mathrm{D}/\mathrm{D}t)$ of point flow quantities. In steady mean flows, since $\partial/\partial t = 0$, for any scalar mean quantity ϕ, $\mathrm{D}\phi/\mathrm{D}t = \nabla\phi \cdot \boldsymbol{U}$. This may be interpreted as the local projection of the gradient of ϕ along the three-dimensional velocity vector or, alternatively, as the pathwise (as opposed to streamwise, which henceforth refers specifically to the Cartesian x direction) change in the quantity ϕ. The left portion of the Fig. 6c frame exhibits $\nabla\rho \cdot \boldsymbol{U}$, which is interpreted as the instantaneous change in density experienced by particles passing through the plane. Positive values of this quantity are compressions—density increasing—whereas negative values denote expansions—density decreasing. Focusing on the downstream side, i.e., between the inviscid shock and the fin, the Fig. 6c frame indicates two regions of expansion: one, a circular-shaped region in the vicinity of the triplepoint (E1) and the other (E2) a relatively thin layer near the plate surface extending approximately between the line of attachment to the trace of the inviscid shock on the plate. The fluid between these two regions of expansion undergoes compression (C). Plots on a conical surface show similar behavior for $\nabla\rho \cdot \boldsymbol{U}$. A typical particle processed just beneath the triplepoint passes successively (i.e., at subsequent streamwise locations) through the separation and rear shocks, expands through E1, moves down toward the plate through C, and then moves spanwise through E2 before separating either from the downstream side of PLS (vortex interaction flow) or the fin side of SLS (entrainment flow).

Further analysis of the quantity $\nabla|U| \cdot \boldsymbol{U}$ (not shown) indicates that fluid in the essentially rotational inviscid upper expansion (E1) and in the compression region (C) experiences increases and decreases, respectively, in velocity magnitude. The situation is more complex in the lower expansion region (E2), occurring in the highly viscous region near the plate, where some portions away from the surface show increases in velocity magnitude, but decreases are evident close to the surface. Nevertheless, as shown in the left portion of the Fig. 6d frame, the spanwise component of velocity is enhanced significantly near the surface. (From the Fig. 6d frame onward, the separating boundary-layer trace on the symmetry plane is plotted in black to show the position of the BLVI shear layer.) Thus, the entrainment flow, after attachment at the PLA, encounters a favorable spanwise pressure gradient component and forms a wall-jetlike structure sweeping toward the symmetry plane. This is shown in the Fig. 6e frame where selected velocity vectors are plotted along plate-normal lines at several locations on the trajectory of a typical surface streamline (red). As displayed in the left portion of the Fig. 6f frame, the Mach numbers in this wall-jetlike structure are very high and show a sharp decrease across the base of the reflected separation shock 6, explaining the higher strength of 6 near the surface. The existence of this wall-jetlike feature in conjunction with the new nature of the boundary layer that originates at PLA near the fin–plate juncture accounts for the absence of significant shock-wave/boundary-layer interaction features here. Close examination of the surface streamlines computed by the RBL method reveals a small streamwise turn in the vicinity of the base of the reflected separation shock. This is accompanied by a local drop in C_f associated with the shock-wave/boundary-layer interaction referred to in the earlier discussion of Fig. 3.

The turning caused by the reflected separation shock is insufficient to align the fluid velocity with the symmetry plane and the wall-jetlike structure persists and ultimately impinges on the symmetry plane. Because of the continuity constraints, the fluid velocity component in the spanwise direction diminishes drastically and vanishes on the symmetry plane. This stagnation process is manifested as a shock—marked previously as the plate centerline structure, PCS—that turns the fluid stream upward (away from the plate) and downstream. The new boundary layer, developing after the entrainment flow attaches at PLA, separates at SLS due to this adverse gradient and accounts for the local minimum in C_f closest to the symmetry plane (Fig. 3).

The velocity magnitude (left side of Fig. 6g frame) shows similar behavior as Mach number with rapid declines occurring through the reflected separation shock (6) and the shock PCS. The entrainment process brings in high-speed fluid near the plate including near the centerline. The stagnation pressure (left side of Fig. 6h frame) also similarly shows a region of low energy beneath the BLVI shear layer. The particle trace shown is colored by local P_t values and is typical of the entrainment flow, originating from the outer portion of the

incoming boundary layer near the fin, approaching the plate, and ultimately arriving near the symmetry plane.

In the Fig. 6i and 6j frames, the structure of the vorticity field is briefly examined. On the crossflow plane of the Fig. 6i frame, the largest values of vorticity occur in the fin and plate boundary layers. However, the range plotted is designed to highlight the structure outside of these regions, where two distinct areas of local maxima are observed, both in the vicinity of the symmetry plane. The top portion forms an arc spanning the centerline and occurs in a region surrounding the separation surface BL shown in the Fig. 6a frame. The dominant component of vorticity in this region is ω_z, i.e., the same as in the upstream boundary layer. On the symmetry plane ω_z is the only possible component of vorticity. The lower region of high vorticity extends between the plate in the vicinity of the SLS to the upper arc. The ω_z is relatively small in this region compared to ω_x and ω_y. This fluid is constituted primarily of the entrainment flow that as observed earlier turns upward and streamwise after separation from SLS spiraling in a complex fashion in the process.

Typical vortex lines colored by vorticity magnitude are shown in the Fig. 6j frame and are consistent with the preceding discussion. In the upstream region, vortex lines extend from the right fin to the left and are parallel to the plate because of the two-dimensional nature of the incoming boundary layer. In the interaction region, the vortex lines form symmetric hairpin shapes, tracing the distance down the right fin and toward the central portion of the interaction, where they bend forward and upward (turning motion of the entrainment flow) and smoothly intersect the symmetry plane along its perpendicular (displaced incoming boundary layer).

In the Fig. 6k frame, the genesis of the high-pressure region near the corner is investigated. In the left portion of the Fig. 6k frame, $|\nabla p|$ values on the plate show the base of the reflected separation shock 6 traversing toward the fin in the downstream direction. This intersects with a new feature that originates from the fin and heads toward the symmetry plane. The formation of this high-gradient region is linked to the impingement of the combined shock at a downstream location. The consequent shock-wave/fin boundary-layer interaction results in increased upstream influence particularly in the low-speed fluid near the fin–plate juncture as observed in the Fig. 6k frame. The details of this interaction may be influenced by the present assumption that the fin boundary layer is turbulent from the fin leading edge. The fin surface streamlines with the RBL method (left portion of the Fig. 6k frame) demonstrate a line of coalescence on the fin near the fin–plate juncture. Thus, whereas the computation and experiment agree that the fin boundary layer is disturbed upstream of inviscid shock impingement, in the computation this is associated with the upstream influence of the corresponding shock-wave/fin boundary-layer interaction rather than the impingement of 6 itself at this location.

The explanation for the disappearance of the triplepoint in the later portion of the interaction is directly based on the structure of the flow presented in the Fig. 6a frame. At downstream crossflow planes, the regions of large flow shear are primarily restricted to the vicinity of the roughly circular region of low total pressure in the central portion of the channel and in relatively shallow new boundary layers on the fin and plate surfaces. This is evident from several of the figures including Fig. 4 and the Fig. 6g and 6h frames. The fluid immediately outside the fin boundary layer in such downstream locations is part of the entrainment flow and has previously been processed through the primary inviscid shock (3). As such, it is relatively uniform. As the cutting plane is moved downstream of the inviscid shock intersection, the trace of the distorted λ successively moves toward the fins encountering flow of lower shear that can be turned parallel to the symmetry plane by a single albeit curved shock (9) as opposed to a λ system. This discrepancy between experiment and computation deserves further study.

This discussion concludes with an examination of the flowfield on the symmetry plane. The limiting trace of the intersection of the shock pattern on the symmetry plane is sketched schematically in Fig. 8. The angle formed by the Mach stem 7 with the plate is roughly 24.5 deg, which lies within 1 deg of the experimental estimate of 23.6 deg.[10] The flow is clarified in the Fig. 6l frame, showing the quantity $\nabla p \cdot \boldsymbol{U}$, the BLVI shear layer, and select velocity vectors

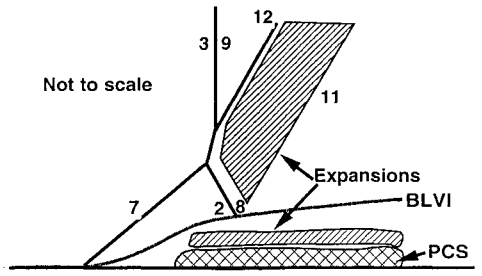

Fig. 8 Limiting shock structure on symmetry plane.

on the symmetry plane. The quantity $\nabla p \cdot \boldsymbol{U}$ is interpreted in the same fashion as $\nabla \rho \cdot \boldsymbol{U}$ for this purpose. Since the spanwise velocity is zero on this plane, the length of these vectors is proportional to the velocity magnitude. In the vicinity of the shear layer and neglecting regions extremely close to the walls, a locally wakelike velocity (magnitude) profile is observed. The smallest velocities occur just beneath the BLVI shear layer because fluid near the plate is accelerated by the infusion of high-speed entrainment flow from the sides. This motion has a large vertical component, i.e., fluid moves away from the plate and out of PCS, thus undergoing an expansion visible just above PCS. The fluid then aligns with BLVI.

Above the BLVI shear layer, the pattern of Fig. 8 displays several characteristics of two-dimensional interactions. The Mach stem 7 deflects the separating boundary layer upward while compressing it. The trace of the rear shock (2, 8) reduces this upward pitch but with further compression. Some of this fluid experiences lower entropy losses compared to that passing through the inviscid shock reflection. As a result, at about one boundary layer height above the location of the BLVI shear layer, a jet is formed (i.e., the velocity magnitude exhibits a local maximum) composed of locally high-energy fluid. Further, the fluid passing through the traces of the rear (2, 8) and inviscid (3, 9) shocks is not aligned with the BLVI shear layer. This displacement effect of the BLVI shear layer is accounted for in the far field by the combination of the centerline shock (12) and the subsequent expansion (11). In the computed domain, 11 ends when the fluid is approximately aligned with the BLVI shear layer.

V. Conclusions

The flowfield structure caused by a Mach 4 double-fin turbulent interaction is examined with two algorithms differing vastly in their properties and historical development: 1) a high-resolution upwind scheme coupled with an algebraic model and 2) a central difference scheme with a k–ϵ model. Deficiencies in the ability of these models to predict surface loading are quantified. Both schemes compare well with experimental data for surface pressure, but the k–ϵ model shows much better trends, especially in skin friction data. Good agreement is also obtained for pitot pressures within the flowfield. Despite large differences in eddy viscosity, the flow structure obtained is independent of method employed and is similar to previous results at Mach 8. The flowfield is described in terms of four regimes: a separated boundary layer, a vortex interaction, a centerline vortex pair, and a high-speed entrainment. These features are related to the computed shock-wave structure that also shows reasonable agreement with experimental visualizations in most regions. This detailed description not only aids in the understanding of inlet flowfields but may be employed to analyze mechanisms of flow control.

Acknowledgments

The authors thank Miguel Visbal for many helpful conversations. We thank also C. C. Horstman for making available the experimental data in a convenient and timely fashion and T. J. Garrison for assistance in its interpretation. The permission of T. J. Garrison and G. S. Settles to use Fig. 5a from Ref. 10 is acknowledged. These calculations were performed at the Department of Defence High Performance Computing Center at the U.S. Army Corps of Engineers Waterways Experiment Station, Vicksburg, MS, as well as at the Numerical Aerodynamic Simulation Facility (NAS).

References

[1]Mee, D., and Stalker, R., "Investigation of Weak Shock-Shock and Shock-Expansion Intersection in the Presence of a Turbulent Boundary Layer," AIAA Paper 87-0549, Jan. 1987.

[2]Settles, G. S., and Dolling, D. S., "Swept Shock/Boundary-Layer Interactions: Tutorial and Update," AIAA Paper 90-0375, Jan. 1990.

[3]Knight, D., Horstman, C., Shapey, B., and Bogdonoff, S., "Structure of Supersonic Turbulent Flow Past a Sharp Fin," *AIAA Journal*, Vol. 25, No. 10, 1987, pp. 1331–1337.

[4]Kubota, H., and Stollery, J., "An Experimental Study of the Interaction Between a Glancing Shock Wave and a Turbulent Boundary Layer," *Journal of Fluid Mechanics*, Vol. 116, 1982, pp. 431–458.

[5]Gaitonde, D., and Knight, D., "Numerical Investigation of Some Control Methods for 3-D Turbulent Interactions Due to Sharp Fins," AIAA Paper 89-0360, Jan. 1989.

[6]Narayanswami, N., Horstman, C. C., and Knight, D. D., "Computation of Crossing Shock/Turbulent Boundary Layer Interaction at Mach 8.3," *AIAA Journal*, Vol. 21, No. 8, 1993, pp. 1369–1376.

[7]Gaitonde, D., and Shang, J. S., "Calculations on a Double-Fin Turbulent Interaction at High Speed," AIAA Paper 93-3432, Aug. 1993; also Gaitonde, D., Shang, J., and Visbal, M., "Structure of a Double-Fin Turbulent Interaction at High Speed," *AIAA Journal*, Vol. 33, No. 2, 1995, pp. 193–200.

[8]Garrison, T. J., and Settles, G. S., "Flowfield Visualization of Crossing Shock-Wave/Boundary Layer Interactions," AIAA Paper 92-0750, Jan. 1992.

[9]Kussoy, M. I., and Horstman, K. C., "Intersecting Shock-Wave/Turbulent Boundary Layer Interactions at Mach 8.3," TR 103909, NASA-TM, Feb. 1992.

[10]Garrison, T. J., and Settles, G. S., "Interaction Strength and Model Geometry Effects on the Structure of Crossing-Shock Wave/Turbulent Boundary-Layer Interactions," AIAA Paper 93-0780, Jan. 1993.

[11]Garrison, T. J., Settles, G. S., Narayanswami, N. N., and Knight, D. D., "Structure of Crossing Shock-Wave/Turbulent-Boundary-Layer Interactions," *AIAA Journal*, Vol. 31, No. 12, 1993, pp. 2204–2211.

[12]Rizzetta, D. P., "Numerical Simulation of Turbulent Cylinder Juncture Flowfields," AIAA Paper 93-3038, June 1993.

[13]Settles, G. S., and Dodson, L. J., "Hypersonic Shock/Boundary-Layer Interaction Database: New and Corrected Data," TR 177638, NASA-CR, May 1994.

[14]York, B., "Evaluation of the Baldwin–Lomax Turbulence Model for a Class of Boundary Layer Flows," M.S. Thesis, Mechanical and Aerospace Engineering Dept., Rutgers Univ., Piscataway, NJ, Oct. 1984.

[15]Rizzetta, D. P., and Visbal, M. R., "Comparative Numerical Study of Two Turbulence Models for Airfoil Static and Dynamic Stall," *AIAA Journal*, Vol. 31, No. 4, 1993, pp. 784–786.

[16]Garrison, T. J., and Settles, G. S., "Laser Interferometer Skin-Friction Measurements of Crossing-Shock Wave/Turbulent Boundary-Layer Interactions," AIAA Paper 93-3072, June 1993; also Garrison, T. J., Settles, G. S., Narayanswami, N., and Knight, D., *AIAA Journal*, Vol. 32, No. 6, 1994, pp. 1234–1241.

[17]Gaitonde, D., and Shang, J. S., "The Structure of a Double-Fin Turbulent Interaction at Mach 4," AIAA Paper 94-2810, June 1994.

[18]Dallmann, U., "Three-Dimensional Vortex Structures and Vorticity Topology," *Fluid Dynamics Research*, Vol. 3, 1988, pp. 183–189.

[19]Alvi, F. S., and Settles, G. S., "Physical Model of the Swept Shock Wave/Boundary-Layer Interaction Flowfield," *AIAA Journal*, Vol. 30, No. 9, 1992, pp. 2252–2258.

[20]Knight, D., Badekas, D., Horstman, C., and Settles, G., "Quasi-conical Flowfield Structure of the Three-Dimensional Single Fin Interaction," *AIAA Journal*, Vol. 30, No. 12, 1992, pp. 2809–2816.

Color reproduction courtesy of U.S. Air Force Wright Laboratory